SDO/AIA and *Hinode*/EIS Observations of Interaction Between an EUV Wave and Active Region Loops

Liheng Yang[1], Jun Zhang[1], Wei Liu[2], Ting Li[1] and Yuandeng Shen[3]

ABSTRACT

We present detailed analysis of an extreme ultraviolet (EUV) wave and its interaction with active region (AR) loops observed by the *Solar Dynamics Observatory*/Atmospheric Imaging Assembly and the *Hinode* EUV Imaging Spectrometer (EIS). This wave was initiated from AR 11261 on 2011 August 4 and propagated at velocities of 430–910 $\mathrm{km\,s^{-1}}$. It was observed to traverse another AR and cross over a filament channel on its path. The EUV wave perturbed neighboring AR loops and excited a disturbance that propagated toward the footpoints of these loops. EIS observations of AR loops revealed that at the time of the wave transit, the original redshift increased by about 3 $\mathrm{km\,s^{-1}}$, while the original blueshift decreased slightly. After the wave transit, these changes were reversed. When the EUV wave arrived at the boundary of a polar coronal hole, two reflected waves were successively produced and part of them propagated above the solar limb. The first reflected wave above the solar limb encountered a large-scale loop system on its path, and a secondary wave rapidly emerged 144 Mm ahead of it at a higher speed. These findings can be explained in the framework of a fast-mode magnetosonic wave interpretation for EUV waves, in which observed EUV waves are generated by expanding coronal mass ejections.

Subject headings: Sun: activity — Sun: corona — Sun: coronal mass ejections (CMEs) — Sun: flares

[1]Key Laboratory of Solar Activity, National Astronomical Observatories, Chinese Academy of Sciences, Beijing 100012, China; [yangliheng;zjun;liting]@bao.ac.cn

[2]W. W. Hansen Experimental Physics Laboratory, Stanford University, Stanford, CA 94305, USA

[3]Kwasan and Hida Observatories, Kyoto University, Kyoto 607-8471, Japan

1. Introduction

Large-scale wave-like coronal disturbances were first discovered by the Extreme Ultraviolet (EUV) Imaging Telescope (EIT; Delaboudinière et al. 1995) on board the *Solar and Heliospheric Observatory* (*SOHO*), and were dubbed EIT or EUV waves (Moses et al. 1997; Thompson et al. 1998). Generally, EUV waves appear as broad, diffuse bright features followed by expanding dimming regions. Early *SOHO*/EIT observations indicated typical EUV wave velocities of 200–400 $\mathrm{km\,s^{-1}}$ (Thompson et al. 1999; Klassen et al. 2000; Thompson & Myers 2009), while a recent statistical study (Nitta et al. 2013) revealed a much higher average velocity of $\sim$600 $\mathrm{km\,s^{-1}}$ for more than 140 EUV waves observed at high cadence by the Atmospheric Imaging Assembly (AIA; Lemen et al. 2011) on board the *Solar Dynamics Observatory* (*SDO*; Pesnell et al. 2012). EUV waves usually originate from flaring active regions (ARs) but have a strong association with coronal mass ejections (CMEs) (e.g., Biesecker et al. 2002; Patsourakos et al. 2009; Chen 2009; Ma et al. 2011; Cheng et al. 2012). Since their discovery, the nature of EUV waves has been strongly debated. Several models have been proposed that can be grouped into wave, non-wave and hybrid wave interpretations. The wave interpretation considers that EUV waves are real waves, including fast-mode magnetohydrodynamic (MHD) waves or shock waves (e.g., Wang 2000; Wu 2001; Schmidt & Ofman 2010), slow-mode MHD waves (Wang et al. 2009a) and soliton waves (Wills-Davey et al. 2007). Among them, the fast-mode MHD wave model is the most popular and supported by many observations (Warmuth et al. 2001; Veronig et al. 2008; Kienreich et al. 2009; Gopalswamy et al. 2009; Patsourakos & Vourlidas 2009; Patsourakos et al. 2009; Liu et al. 2011; Zheng et al. 2011; Asai et al. 2012). The non-wave interpretation refers to EUV waves as signatures of a current shell or successive restructuring of field lines during a CME (Delannée 2000; Delannée et al. 2008; Chen et al. 2002; Attill et al. 2007; Schrijver et al. 2011). The hybrid wave model points out that wave and non-wave phenomena, which might represent different physical processes, could co-exist in a single event, and there is no need to develop a unified wave model to explain all the observational characteristics of EUV waves (Zhukov & Auchère 2004; Cohen et al. 2009; Downs et al. 2011; Chen et al. 2002, 2005). More recent high resolution observations are inclined to support this interpretation (Liu et al. 2010, 2012; Li et al. 2012). Comprehensive reviews of these models and observations can be found in Wills-Davey & Attrill (2009), Warmuth (2010), Gallagher & Long (2011), Zhukov (2011) and Patsourakos & Vourlidas (2012).

EUV waves have been observed to interact with various coronal structures in their paths, such as coronal holes (CHs), ARs and coronal loops. Early observations revealed that EUV waves could not travel across ARs (Wills-Davey & Thompson 1999), and stopped or partially intruded into CHs (Thompson et al. 1998, 1999; Veronig et al. 2006). This was independently confirmed by numerical simulations of Wang (2000), Wu (2001) and

Ofman & Thompson (2002). EUV waves were observed by the EUV Imagers (EUVI; Wuelser et al. 2004) on board the *Solar-Terrestrial Relations Observatory* (*STEREO*; Kaiser et al. 2008) to be reflected from CHs (Gopalswamy et al. 2009). This was further confirmed from higher cadence and sensitivity observations by *SDO*/AIA (Li et al. 2012; Shen & Liu 2012). Combining observations from *STEREO*/EUVI and *SDO*/AIA, Olmedo et al. (2012) investigated an EUV wave and its interaction with a CH over the entire solar surface. They found that part of the EUV wave transmitted through the CH, and the loop arcade at the CH boundary triggered a secondary wave, which appeared to have been reflected. Secondary waves produced by distorted AR magnetic field have been simulated by Ofman & Thompson (2002), and then observationally confirmed by Li et al. (2012). Additionally, EUV waves were reported to interact with coronal loops (Thompson et al. 1998; Delannée & Aulanier 1999; Delannée 2000). Wills-Davey & Thompson (1999) found in *Transition Region and Coronal Explorer* (*TRACE*) observations that an EUV wave propagated through diffuse, overarching coronal loops and triggered their transverse oscillations with a maximum displacement of 6 Mm and velocity amplitudes of 15–20 $\mathrm{km\,s^{-1}}$. Similar phenomena were observed by *SDO*/AIA (Aschwanden & Schrijver 2011; Schrijver et al. 2011; Liu et al. 2012; Shen & Liu 2012). In addition, filament oscillations can be triggered by the passage of an EUV wave (Okamoto et al. 2004; Hershaw et al. 2011) or Moreton wave (Gilbert et al. 2008).

Spectroscopic observations can provide plasma diagnostics of EUV waves and help to clarify their nature. However, such observations are very rare due to the difficulty of aiming a narrow slit at the location where a coronal wave will propagate (Zhukov 2011). Harra & Sterling (2003) performed the first spectroscopic analysis of an EUV wave event with the Coronal Diagnostic Spectrometer (CDS) instrument on board *SOHO*. In their observations, a weak wave front passed the CDS field of view but showed no significant Doppler velocities ($\lesssim 10\ \mathrm{km\,s^{-1}}$). By using the Extreme-Ultraviolet Imaging Spectrometer (EIS; Culhane et al. 2007) on board *Hinode*, Chen et al. (2011) studied the interaction between an EIT wave and a coronal upflow region by using *Hinode*/EIS, and the upflow and non-thermal velocities were found to diminish after the passage of the wave front. They suggested that this phenomenon implied changes of magnetic field orientation, and was consistent with the field line stretching model of EUV waves. Recently, a unique data set was obtained during the *Hinode* Observing Plan HOP-180 by placing a slit on the path of an EUV wave. Using these data, Harra et al. (2011) found two redshift signatures corresponding to the wave pulses. They propagated along the EIS slit with an average velocity of $\sim$500 $\mathrm{km\,s^{-1}}$, which was similar to the velocity of the associated wave front observed by *SDO*/AIA. They considered that these redshifts might be signatures of plasma pushed downward and compressed by a coronal MHD wave. In the followup work of the same event, Veronig et al. (2011) found that a redshift of 20 $\mathrm{km\,s^{-1}}$ was followed by a blueshift of $-5\ \mathrm{km\,s^{-1}}$, indicating

relaxation of the plasma behind the wave front. Both studies concluded that the observed wave was a coronal fast-mode MHD wave being generated by the outgoing CME.

In this paper, we present detailed analysis of an EUV wave observed simultaneously by both *SDO*/AIA and *Hinode*/EIS that sheds new light on its interaction with AR loops and CHs. We describe the observations in Section 2 and present analysis results in Sections 3 and 4, followed by conclusions and discussion in Section 5.

2. Observations and Data Analysis

On 2011 August 4, AR 11261 produced an M9.3 class flare at the location of N16°W49°, which started at 03:41 UT and peaked at 03:57 UT. Following the onset of the flare, we observed an EUV wave, a filament eruption and a fast halo CME of 1315 $\mathrm{km\,s^{-1}}$. The EUV wave was well observed by *SDO*/AIA. AIA can provide high resolution (1.5″), high cadence (12 s) full-disk images of the corona and transition region up to 0.5 $\mathrm{R_\odot}$ above the solar limb. AIA images are taken in seven EUV passbands and three continuum bands, the former of which are centered at specific lines: Fe XVIII (94 Å), Fe VIII,XXI (131 Å), Fe IX (171 Å), Fe XII,XXIV (193 Å), Fe XIV (211 Å), He II (304 Å), and Fe XVI (335 Å), covering a wide temperature range from 6×10^4 to 6×10^7 K. This EUV wave was recorded by all of the seven EUV channels. However, only four channels ((171, 193, 211, and 335 Å) were analyzed in detail, in which the EUV wave was more evident.

At about 04:01 UT, the eastern part of the EUV wave propagated to AR 11263 (N17°W18°) and was captured by *Hinode*/EIS. EIS observes the solar corona and upper transition region in two EUV wavebands: 170–210 Å and 250–290 Å. It has a spatial resolution along the slit of 1″ $\mathrm{pixel^{-1}}$ and a spectral resolution of 0.0223 Å $\mathrm{pixel^{-1}}$, which permits Doppler velocity measurements better than 5 $\mathrm{km\,s^{-1}}$. Two spectral slits (1″ and 2″) provide high-resolution spectra and two imaging slots (40″ and 266″) provide monochromatic images. In the present work, the 2″ slit was used to scan an area of 240″×16″ with 25 s exposure time, giving an averaged duration of about 3.5 min. We used the EIS data during the period of 02:07–04:46 UT, including 19 continuous observation sequences from 03:45 UT to 04:46 UT, which allows us to study the plasma behavior before, during, and after the EUV wave. However, the 04:39 UT and 04:40 UT sequences were only partially scanned and not included in this study. Each sequence contained nine spectral windows, but our study mainly concentrated on two emission lines (Fe XII 195.12 Å and Fe XIII 202.04 Å), whose maximum response temperatures were respectively 1.2 and 1.6 MK. In addition, Si X 258.37 and 261.04 Å lines, which have the same maximum response temperature **as** the Fe XII line, were also chosen to make the density diagnosis.

We processed the raw EIS data by using the standard routine eis_prep.pro in the SolarSoftWare (SSW) packages (Freeland & Handy 1998), which corrected the data for cosmic ray hits, hot pixels, detector bias and dark current. Then we used eis_auto_fit.pro with a single Gaussian model to obtain spectral intensities, line widths and Doppler velocities. From the Si X λ258.37/λ261.04 line pair, we derived the coronal electron densities (Dere et al. 1997).

AIA images were first differentially de-rotated to a common time at 05:00 UT and then running differenced by subtracting the previous image in time. We adopted a semi-automatic approach (Podladchikova & Berghmans 2005; Liu et al. 2010; Li et al. 2012) to track the wave propagation. As shown in Figure 1, for the primary EUV wave on the solar disk, we defined the eruption center (N14°W38°) as the new "north pole" from which three heliographic "longitudinal" sectors (labeled "A"–"C") of 10° wide were selected. For each sector in an image, we averaged pixels in the perpendicular ("latitudinal") direction and obtained a one-dimensional profile as a function of spherical distance measured along the "longitudinal" great circle (thus accounting for the Sun's sphericity). The distance step size along the sector was selected to correspond to AIA's pixel size of 0.6″. Repeating this for a sequence of images and aligning the resulting profiles over time gave a two-dimensional time-distance plot. Likewise, for the reflected EUV wave from AR 11263 (N11°W9°), we defined Sectors "D"–"F" of the same size centered there. For the secondary wave above the southeast limb, we selected a cut of a right triangular shape (labeled "G"), from which pixels were averaged in the direction along the shortest side (from "v1" to "v2" in Figure 1).

The wave front was identified as a bright or dark track in the time-distance plot. To measure its velocity (acceleration), we first determined that whether its slope was uniform. If it was uniform, we applied a linear (parabolic) fit to it. Otherwise, we divided it according to its slope, and then applied a linear (parabolic) fit to the linear (non-linear) segment. For a certain wave front, dozens of data points were chosen along the front of the wave pulse at a set time interval (marked by blue dotted lines in Figures 3–5). We performed linear (parabolic) fit to these data points, repeated measurements ten times and then took average as the final velocity (acceleration). The error was the standard deviation from the multiple measurements.

3. AIA Observations of the EUV Wave

3.1. Overview of the EUV Wave

Figure 2 displays the evolution of the EUV wave in the 211 Å channel. The pre-event intensity map at 03:40:00 UT clearly shows that there are a series of coronal loops (marked by

"L1" in Figure 2(a)) connecting ARs 11261 and 11263. To the southeast of AR 11263, three small-scale coronal structures, where reflected waves are observed, are identified with "S1", "S2" and "S3". The corresponding reflected waves are marked by "R1" , "R2" and "R3" (see Figures 2(e) and (f)). The position of the EIS slit is superimposed on this image (see the white box in Figure 2(a)), and is close to L1. The upper part of the slit was dominated by the strong background emission in the core of AR 11263, so it is difficult to determine whether the wave passes through it or not. Hence, only observations from the lower part of the slit, shown as the black box in Figures 2(b)–(f), were used for our analysis. The running difference images in Figure 2 clearly show the propagation of the EUV wave.

As a typical feature of EUV wave events, erupting loops (marked by "L2" in Figure 2(b)) behind the EUV wave were observed (e.g., Liu et al. 2010; Li et al. 2012). They appeared as semicircular bright arcades straddling AR 11261 and began to expand to the northwest at 03:48:00 UT. Three minutes later, a diffuse EUV wave pulse appeared ahead of it. Initially, it mainly spread to the northwest, consistent with the orientation of L2 (see Animations 1 and 2). In other directions, the EUV wave was relatively weak. We note that the loops to the south of AR 11261 (marked by "L3" in Figure 2(c) and Figure 3(b)) were disturbed, and it became more extended and brighter. Seen from the time-distance plot of Sector "A", some of L3 returned to their original position after the EUV wave passed over, indicating oscillations triggered by the impact of the EUV wave (e.g., Patsourakos et al. 2009; Aschwanden & Schrijver 2011; Liu et al. 2012). By 03:54:24 UT, the EUV wave developed to a semi-circular shape (Figure 2(c)), with a deformation in its eastern part, an indicator of the interaction of the EUV wave with L1, which became increasingly evident as the EUV wave evolved.

To quantify the EUV wave kinematics, we used three time-distance slices along Sectors "A"–"C". As seen from Figures 2 and 3, the EUV wave appeared as bright tracks in the hotter 193, 211 and 335 Å channels, while a dark track in the cooler 171 Å channel, suggesting plasma heating (Wills-Davey & Thompson 1999; Liu et al. 2010, 2012; Long et al. 2011a; Ma et al. 2011; Li et al. 2012). In the 211 channel, the average propagation velocities of this EUV wave were from (448±9) to (900±10) $\mathrm{km\,s^{-1}}$ in the three directions. We note that in the same direction, the EUV wave displayed similar velocities in the four channels and the velocity differences were almost within the error range except for the velocity of Sector "B" in the 171 Å channel, which was lower than those in the other three channels. This might be due to the fuzzy wave front. For Sector "A", the EUV wave exhibited a deceleration between 400 Mm and 500 Mm from the eruption center (Figures 3(b)–(e)). A parabolic fit to the EUV wave within this distance revealed a deceleration of (1010±80)–(1060±70) $\mathrm{m\,s^{-2}}$. In sector "C", the EUV wave velocity decreased to (270±20)–(301±6) $\mathrm{km\,s^{-1}}$ at about 440 Mm from the eruption center (marked by the white dash-dotted line in Figures 4(a)–(e)).

In order to validate the measured EUV wave kinematics, we compared velocities and accelerations measured from Sector "A" in the running difference stack plots (Figures 3(b)–(e)) with those in the base difference stack plots (Figures 3(b1)–(e1)), which had the base time at 03:40 UT. For the base difference stack plots, the velocities and accelerations of the EUV wave were measured along the center other than the front of the wave pulse. It is noted that the velocities of the same feature measured from the two methods had little difference. In addition, the deceleration between 400 Mm and 500 Mm from the eruption center measured from the base difference stack plots was (980±70)–(1060±90) $\mathrm{m\,s^{-2}}$, which was consistent with that measured from running difference stack plots.

3.2. Interaction of the EUV Wave with Nearby Inter-AR Loops

In order to clearly describe the interaction between the EUV wave and L1, we divide the interaction into two phases. The first phase was from 03:52:00 to 04:00:24 UT, that is, before the EUV wave reached the apex of L1. During this phase, the EUV wave moved through L1 at a velocity of (430±10)–(448±9) $\mathrm{km\,s^{-1}}$ (Figures 4(a)–(e); Animations 3 and 4), and the wave front had a deformation. Similar observations were reported by Wills-Davey & Thompson (1999), Delann*é*e & Aulanier (1999) and Delann*é*e (2000).

The second phase ranged from 04:00:24 to 04:10:00 UT. At 04:00:24 UT, the EUV wave arrived at the apex of L1, and excited a disturbance in L1 (see Figure 2(d)). Then, the EUV wave and the disturbance formed a clear bifurcation in the space-time plot (Figure 2(d); the top and middle rows of Figure 4). Such bifurcation was obvious in the 211, 193 and 335 Å channels, but not observed in the 171 Å channel. Simultaneously, the EUV wave pushed L1 forward (see Animation 3). L1 showed motions parallel to their magnetic field structure, different from the observations of Wills-Davey & Thompson (1999), in which the disrupted coronal loops showed motions perpendicular to their magnetic field structure. Seen from the time-distance plot of Sector "C", the velocity of L1 was about (64±3)–(97±7) $\mathrm{km\,s^{-1}}$. This movement lasted about 10 min, leading to a maximum displacement of about 37–62 Mm. About 14 min later, another bright signal appeared at the apex of L1 (Figure 2(f) and Figures 4(a), (b), (d), and (e); Animation 3). It had a lower velocity of about (37±2)–(58±5) $\mathrm{km\,s^{-1}}$, but lasted a much longer time (about 15 min), giving a maximum displacement of about 32–57 Mm.

At the same time, the disturbance gradually propagated toward the footpoints of L1 (Animations 3 and 4). As seen from the time-distance plot of Sector "D", it moved at a velocity of about (179±9)–(220±10) $\mathrm{km\,s^{-1}}$. At 04:10:00 UT, it reached the footpoints of L1.

3.3. Passage of the EUV Wave Through AR 11264 and a Filament Channel

At 03:55:36 UT, the EUV wave encountered a coronal bright point (see Figure 1, also indicated by the black dashed line in Figure 3). Part of it just passed over this bright point while the rest of the wave front was deformed. Seen from the time-distance plot of Sector "A", the EUV wave split into two branches, with a time delay of about 2 min. We note that the two branches had similar velocities in the four AIA channels, (590±10)–(621±8) $\mathrm{km\,s^{-1}}$ for the leading front, (590±20)–(600±20) $\mathrm{km\,s^{-1}}$ for the trailing front. At 04:03 UT, the EUV wave passed through AR 11264 (see Figure 1 and white dot-dashed line in Figure 3) rather than stopping at its boundary. As seen from the time-distance plot of Sector "A", the velocity of the EUV wave in this AR was about (760±20)–(760±30) $\mathrm{km\,s^{-1}}$, larger than the original velocity, consistent with the result of Li et al. (2012). This phenomenon can be clearly seen in the 211 and 193 Å channels, weak in the 335 Å channel, and not observed in the 171 Å channel.

At 04:54:00 UT, the EUV wave arrived at the boundary of a filament channel, which was located between 330 Mm and 420 Mm from the eruption center in Sector "B" (see Figure 1 and white dashed lines in Figure 3). It is noted that the EUV wave directly crossed over the filament channel without any velocity variation.

3.4. Reflected Waves from Coronal Structures

At 04:08:48 UT, the southeast part of the EUV wave encountered some coronal structures in the quiet Sun, S1 and S2 (Figure 2(a)), and produced reflected waves R1 and R2 that propagate toward the north (see Figure 2(e), Figures 5(a) and (e), and Animation 2). Another reflected wave R3 was produced at S3 at 04:16:00 UT. As seen from the time-distance plot of Sector "C" (Figures 4(a)–(e)), R3 appeared as brightening at 211, 193 and 335 Å, but darkening at 171 Å. Its initial velocity was (300±10)–(330±10) $\mathrm{km\,s^{-1}}$, slightly greater than that of the incident wave (about (270±20)–(301±6) $\mathrm{km\,s^{-1}}$). We note that R3 finally propagated into AR 11263, and thus we selected Sectors "E" and "F" to track its late-stage propagation. The resulting time-distance plots are shown in Figure 5, giving R3's final velocities ranging from (99±9) to (137±4) $\mathrm{km\,s^{-1}}$.

Some intensity oscillations, as marked by the short blue line in Figure 1, occurred at S3 in the quiet Sun to the south of AR 11263. They were captured both in Sector "C" at a distance of 500 Mm from the eruption center and in Sector "E" at 300 Mm, as shown in the top panels of Figures 4 and 5. The oscillations, with a period of about 12 minutes, started at about the same time as the reflected wave R3. In addition, as can be seen in

Figure 5 (bottom), subsequent wave pulses appeared after the initial R3 pulse, each delayed by about 12 minutes. This suggests that the multiple R3 wave pulses were generated by the oscillations of the local loops at S3.

3.5. Secondary Wave Excited by the Reflected Wave from a Polar CH

At 04:22:00 UT, the EUV wave arrived at the boundary of the southern polar CH, and then a reflected wave was observed to propagate to the northeast (see Animations 2 and 5). About 1 min later, part of this reflected wave appeared above the solar limb (marked by "RW1" in Figures 6(b)–(e)). Seen from the stack plot of Sector "G", we note that it had a velocity of 400±10 $\mathrm{km\,s^{-1}}$, which was lower than that of the primary wave (621±8 $\mathrm{km\,s^{-1}}$, see Figure 3(b)). At 04:30:00 UT, the reflected wave encountered a large-scale loop system (marked by "Loops" in Figure 6(a)), and a secondary wave (marked by "SW" in Figures 6(c), (d) and (e)) rapidly emerged 144 Mm ahead of it at a higher velocity of 510±20 $\mathrm{km\,s^{-1}}$, in line with that reported by Li et al. (2012). However, instead of disappearing after the secondary wave was generated, the reflected wave continuously propagated forward. These are consistent with secondary waves produced by distorted AR magnetic fields, which were simulated by Ofman & Thompson (2002). At 04:30:24 UT, another reflected wave (marked by "RW2" in Figures 6(c)–(e)) appeared above the solar limb at a velocity of 400±10 $\mathrm{km\,s^{-1}}$. However, this reflected wave disappeared after a certain distance before any interaction with the large-scale loop system was detected.

4. Spectroscopic Analysis of the EUV Wave

Figure 7 shows time sequences of the Doppler velocity and line width images for the Fe XIII and Fe XII lines. At 04:00 UT when the EUV wave arrived, some red-shifted features appeared or were enhanced, being more evident in the hotter Fe XIII line. Simultaneously, the widths of both lines increased. After the EUV wave transit, there were some additional variations in the Doppler velocity. A significant intensity enhancement was expected when the EUV wave swept through the EIS, but was not detected (see Figure 8(e)).

To study the variations of the Doppler velocity and line width in detail, we selected areas "A" and "B" (see Figure 7(a)) that were originally blue-shifted and red-shifted, respectively, and both showed distinct variations during the EUV wave passage. We calculated the averaged Doppler velocity and line width in both areas for the two spectral lines, which are shown as a function of time in Figure 8. At the time of the EUV wave transit, the red-

shifted feature in "B" for the Fe XIII line increased by about 3 $\mathrm{km\,s^{-1}}$ and formed a sharp peak (marked by "vp1" in Figure 8(a)), while the blue-shifted feature in "A" decreased slightly. Similar variations were also noticed in the Fe XII line. Simultaneously, the line width in both "A" and "B" for the two lines clearly increased (marked by "wp1" in Figures 8(b) and (d)). For "B", it increased by about 10 mÅ for the Fe XIII line and about 7 mÅ for the Fe XII line. The line width increases were somewhat smaller in "A", by 6 mÅ and 5 mÅ, respectively.

There are two spikes in Doppler velocity following the initial peak at the time of the EUV wave arrival. They appeared at around 04:10 UT (marked by "vp2" in Figures 8(a) and (c)) and 04:32 UT (marked by "vp3" in Figures 8(a) and (c)), respectively. The first spike seemed to be caused by the disturbance of the EUV wave, while the second spike might be associated with the second peak in line width (marked by "wp2" in Figures 8(b) and (d)), which appeared at 04:21 UT and might not be the result of the EUV wave.

In order to validate the above result, we also study the variation of the Doppler velocity and line width between 02:07 and 03:08 UT. It is noticed that the variation of the Doppler velocity had no clear trend during this period. For "A", the mean Doppler velocity was -1.3 $\mathrm{km\,s^{-1}}$ for the Fe XIII line and -3.0 $\mathrm{km\,s^{-1}}$ for the Fe XII line (marked by the horizontal dash-dotted lines in Figures 8(a) and (c)). For "B", the mean Doppler velocity was 2.9 $\mathrm{km\,s^{-1}}$ for the Fe XIII line and 1.6 $\mathrm{km\,s^{-1}}$ for the Fe XII line. Although the variation of the line width during this period seemed to have periodicity, the variations were within 4 mÅ for the Fe XIII line and within 2 mÅ for the Fe XII line.

Plasma densities, which were derived from the EIS Si X line pair, as a function of time were presented in Figure 8(f). It is noted that the changes of the plasma density were not obvious when the EUV wave passed over. The plasma density decreased by about 2.9×10^8 $\mathrm{cm^{-3}}$ in "A" and 1.1×10^8 $\mathrm{cm^{-3}}$ in "B", which were within the variation range of the plasma density between 02:07 and 03:08 UT. These observational results were similar to those given by Veronig et al. (2011), in which small density changes associated with an EUV wave. We note that after the EUV wave transit, the plasma density reached a peak of 1.8×10^{10} $\mathrm{cm^{-3}}$ in "B" and of 9.1×10^9 $\mathrm{cm^{-3}}$ in "A" , marked by "dp2" and "dp1", respectively. The peak of the plasma density in "A" seemed to be associated with the peak of the Fe XII intensity (marked by "ip") but had a 14 min delay compared with vp1. The peaks of the plasma density and the intensity might be the result of disturbances in AR loops caused by the EUV wave. Phase difference between Doppler velocity and intensity might provide an evidence for the existence of a slow-mode wave (Wang et al. 2009b), indicating that the disturbances were probably slow-mode waves. Moreover, we note that dp1 and dp2 had a time difference of about 7 min, which might imply that their oscillations are not in phase among different

loops.

5. Conclusions and Discussion

We have presented detailed analysis of *SDO*/AIA and *Hinode*/EIS observations of an EUV wave associated with an M9.3 class flare and a fast halo CME, focusing on its interaction with local coronal loops. The main observational results are summarized as follows.

1. The EUV wave had velocities from 430±10 to 910±10 $\mathrm{km\,s^{-1}}$ in different directions. In the northeast direction, it showed a clear deceleration of (1010±80)–(1060±70) $\mathrm{m\,s^{-2}}$. Such deceleration has been shown by multiple authors including Warmuth et al. (2004), Long et al. (2011a,b), Muhr et al. (2011), as well as Ma et al. (2011) and Cheng et al. (2012). According to the extensive statistical study of Warmuth & Mann (2011), the initial wave speeds exceeding 320 $\mathrm{km\,s^{-1}}$ showed pronounced deceleration. They pointed out that the kinematic behavior of the decelerating wave was consistent with nonlinear large-amplitude waves or shocks that propagated faster than the ambient fast-mode wave speed and subsequently slowed down due to decreasing amplitude.

2. The wave front first propagated through nearby inter-AR loops at a velocity of (430±10)–(448±9) $\mathrm{km\,s^{-1}}$. When it arrived at the apex of these loops, it excited a disturbance that finally propagated toward the footpoints of these loops at a velocity of (179±9)–(220±10) $\mathrm{km\,s^{-1}}$. Simultaneously, the EUV wave pushed these AR loops forward with velocities of about (64±3)–(97±7) $\mathrm{km\,s^{-1}}$ and a maximum displacement of about 37–62 Mm. About 14 min later, another bright signal appeared at the apex of these loops. It had a lower velocity of about (37±2)–(58±5) $\mathrm{km\,s^{-1}}$, but lasted a much longer time, giving a maximum displacement of about 32–57 Mm. Such bright signal might be the result of the AR loop oscillation. Previously, propagating disturbances in AR loops were reported by many researchers (e.g., De Moortel et al. 2000; Wang et al. 2009a; McIntosh & De Pontieu 2009; Tian et al. 2011). Such propagating disturbances were similar to our observed disturbance except that they were periodic. The nature of these propagating disturbances **is** still an open question. Some researchers have suggested that the disturbances are mass flows (e.g., McIntosh & De Pontieu 2009; Tian et al. 2011), and the others considered them as slow-mode waves (e.g., De Moortel et al. 2000; Wang et al. 2009b). More recently, Ofman et al. (2012) found that both slow-mode waves and persistent upflows were present in the same impulsive events at the base of ARs based on the results of the 3D MHD model.

3. The EUV wave passed through AR 11264 and a filament channel on its path. This lends support to the fast-mode wave model of EUV waves, but contradicts the prediction

of the non-wave model (Chen et al. 2002) that an EUV wave should stop at a magnetic separatrix between an AR or a filament channel and the rest of the corona. In addition, the velocity of the EUV wave increased by almost 200 km s^{-1} within AR, consistent with expected higher fast-mode wave speeds there. However, in contrast to the velocity increase of an EUV wave detected within a flux rope cavity hosting a filament (Liu et al. 2012), there is no detectable velocity change at the filament channel in our case. We speculate that the associated flux rope cavity in our case could have a similar fast-mode wave speed as the surrounding corona or be situated at a lower height than the EUV wave in the corona.

4. When the EUV wave arrived at the boundary of a polar CH, two reflected waves were successively produced and part of them propagated above the solar limb. The first reflected wave above the solar limb encountered a large-scale loop system on its path, then a secondary wave rapidly emerged 144 Mm ahead of it at a higher speed. This is the first time that a secondary wave produced by a reflected wave is observed. It is consistent with secondary waves produced by distorted AR magnetic fields, which were simulated by Ofman & Thompson (2002). Recently, Li et al. (2012) studied a global EUV wave on 2011 June 7. They found that when the EUV wave arrived at an AR on its path, the primary EUV wave apparently disappeared and a secondary wave rapidly reemerged within 75 Mm of the AR boundary at a similar speed. Similar to their observation, we also observed a secondary wave at a certain distance away from the initial wave. However, our initial wave continuously propagated forward rather than disappearing. It might indicate that the observed secondary wave might be a newly generated wave due to the interaction between the reflected wave and the large-scale loop system. In addition, we observed two reflected waves, which might be triggered by the oscillations of the coronal hole boundary upon the impact of the primary EUV wave and the 8 min delay of the two reflected waves may indicate the oscillation period.

5. EIS observations of AR loops in AR 11263 revealed that at the time of the wave transit, the original red-shifted feature had an increase of about 3 $km\,s^{-1}$, and the original blue-shifted feature slightly weakened. After the wave transit, these changes were reversed. Our results are similar to the recent studies using *Hinode*/EIS and *SDO*/AIA observations (Harra et al. 2011; Veronig et al. 2011). It can be explained by the scenario of a fast-mode wave model as described by Uchida (1968). When the EUV wave encountered the AR loops, it would provide a downward pulse to these loops (e.g., Liu et al. 2012). After the EUV wave transit, these disturbed loops restored to its original state. In addition, we did not detect any evident intensity enhancement among the available EIS lines when the EUV wave swept through the EIS slit. This is consistent with the findings of Chen et al. (2011) who concluded that the variation of line intensity during the wave propagation was within the fitting error, so it is difficult to distinguish such changes from spectroscopic observations. Coronal magnetic field strength of quiet Sun can be calculated through coronal seismology

by measuring the wave speed, coronal density and temperature (West et al. 2011; Long et al. 2013). In our event, though the EIS slit was located in AR 11263, the area in the lower part of the slit was relatively quiet. Hence, the local wave velocity and coronal density can be used to estimate the local magnetic field strength. In order to determine the local wave velocity, we selected a 10° wide sector, which started from the eruption center and intersected the lower part of the EIS slit, and derived a time-distance plot in the 193 Å channel, who had the same maximum response temperature (about 1.2 MK) with the Si X line. The wave velocity was estimated to be 410±20 $\mathrm{km\,s^{-1}}$. We note that when the EUV wave swept through the EIS slit, the plasma density was 5.5×10^8 $\mathrm{cm^{-3}}$ in "A" and 4.4×10^8 $\mathrm{cm^{-3}}$ in "B". The local magnetic field strength can be calculated using $B=(4\pi n(mv_{fm}{}^2\text{-}\gamma k_B T))^{1/2}$, which was deduced by Long et al. (2013). B is the magnetic field strength, v_{fm} is the wave speed, n is plasma density, m is the proton mass, $\gamma=5/3$ is the adiabatic index, k_B is the Boltzmann constant and T is the peak emission temperature of the density sensitive lines. The calculated local magnetic field strength is 1.6±0.2 G in "A" and 1.3±0.1 G in "B".

In summary, we find a series of phenomena associated with the interaction of incident or reflected waves with coronal loops, such as a disturbance in AR loops excited by the EUV wave and a secondary wave generated by the reflected wave from a polar CH. These observational findings can be explained by the fast-mode magnetoacoustic interpretations for EUV waves, in which the observed waves are generated by expanding CMEs.

We thank the anonymous referee for the helpful suggestions and comments. We also thank the *Hinode*/EIS and *SDO*/AIA teams for providing the wonderful data. *Hinode* is a Japanese mission developed and launched by ISAS/JAXA, with NAOJ as domestic partner and NASA and STFC (UK) as international partners. It is operated by these agencies in co-operation with ESA and NSC (Norway). The work is supported by the National Natural Science Funds for Distinguished Young Scholar (11025315), the National Basic Research Program of China under grant 2011CB811403, National Natural Science Foundations of China (10921303, 11103075 and 11203037), and the CAS Project KJCX2-EW-T07.

REFERENCES

Asai, A., Ishii, T. T., Isobe, H., et al. 2012, ApJ, 745, L18

Aschwanden, W., & Schrijver C. J. 2011, ApJ, 736, 102

Attill, G. D. R., Harra, L. K., van Driel-Gesztelyi, L., & Démoulin, P. 2007, ApJ, 656, L101

Biesecker, D. A., Myers, D. C., Thompson, B. J., Hammer, D. M., & Vourlidas, A. 2002, ApJ, 569, 1009

Chen, F., Ding, M. D., Chen, P. F., & Harra, L. K. 2011, ApJ, 740, 116

Chen, P. F. 2009, ApJ, 698, L112

Chen, P. F., Fang, C., & Shibata, K. 2005, ApJ, 622, 1202

Chen, P. F., Wu, S. T., Shibata, K., & Fang, C. 2002, ApJ, 572, L99

Cheng, X., Zhang, J., Olmedo, O., et al., 2012, ApJ, 745, L5

Cohen, O., Attrill, G. D. R., Manchester, W. B., IV, & Wills-Davey, M. J. 2009, ApJ, 705, 587

Culhane, J. L., Harra, L. K., James, A. M., et al. 2007, Sol. Phys., 243, 19

Delaboudinière, J.-P., Artzner, G. E., Brunaud, J., et al. 1995, Sol. Phys., 162, 291

Delannée, C. 2000, ApJ, 545, 512

Delannée, C., & Aulanier, G. 1999, Sol. Phys., 190, 107

Delannée, C., Török, T., Aulanier, G., & Hochedez, J.-F. 2008, Sol. Phys., 247, 123

De Moortel, I., Ireland, J., & Walsh, R. W. 2000, A&A, 355, L23

Dere, K. P., Landi, E., Mason, H. E., Monsignori Fossi, B. C., & Young, P. R. 1997, A&AS, 125, 149

Downs, C., Roussev, I. I., van der Holst, B., et al. 2011, ApJ, 728, 2

Freeland, S. L., & Handy, B. N. 1998, Sol. Phys., 182, 497

Gallagher, P. T., & Long, D. M. 2011, Space Sci. Rev., 158, 365

Gilbert, H. R., Daou, A. G., Young, D., Tripathi, D., & Alexander, D. 2008, ApJ, 685, 629

Gopalswamy, N., Yashiro, S., Temmer, M., et al. 2009, ApJ, 691, L123

Harra, L. K., & Sterling, A. C. 2003, ApJ, 587, 429

Harra, L. K., Sterling, A. C., Gömöry, P., & Veronig A. 2011, ApJ, 737, L4

Hershaw, J., Foullon, C., Nakariakov, V. M., & Verwichte, E. 2011, A&A, 531, A53

Kaiser, M. L., Kucera, T. A., Davila, J. M., et al. 2008, Space Sci. Rev., 136, 5

Kienreich, I. W., Temmer, M., & Veronig, A. M. 2009, ApJ, 703, L118

Klassen, A., Aurass, H., Mann, G., & Thompson, B. J. 2000, A&AS, 141, 357

Lemen, J. R., Title, A. M., Akin, D. J., et al. 2012, Sol. Phys., 275, 17

Li, T., Zhang, J., Yang, S. H., & Liu, W. 2012, ApJ, 746, 13

Liu, W., Nitta, N. V., Schrijver, C. J., Title, A. M., & Tarbell, T. D. 2010, ApJ, 723, L53

Liu, W., Ofman, L., Nitta, N. V., et al. 2012, ApJ, 753, 52

Liu, Y., Luhman, J. G., Bale, S. D., & Lin, R. P. 2011, ApJ, 734, 84

Long, D. M., DeLuca, E. E., & Gallagher, P. T. 2011a, ApJ, 741, L21

Long, D. M., Gallagher, P. T., McAteer, R. T. J., & Bloomfield, D. S. 2011b, A&A, 531, 42

Long, D. M., Williams, D. R., Régnier, S., & Harra, L. K. 2013, in press(arXiv:1305.5169)

Ma, S. L., Raymond, J. C., Golub, L., et al. 2011, ApJ, 738, 160

McIntosh, S. W., & De Pontieu, B. 2009, ApJ, 706, L80

Morses, D., Clette, F., Delaboudinière J.-P., et al. 1997, Sol. Phys., 175, 571

Muhr, N., Veronig, A. M., Kienreich, I. W., Temmer, M., & Vršnak, B. 2011, ApJ, 739, 89

Nitta, N. V., Schrijver, C. J., Title, A. M., & Liu, W. 2013, ApJ, submitted

Ofman, L., & Thompson, B. J. 2002, ApJ, 574, 440

Ofman, L., Wang, T. J., & Davila J. M. 2012, ApJ, 754, 111

Okamoto, T. J., Nakai, H., Keiyama, A., et al. 2004, ApJ, 608, 1124

Olmedo, O., Vourlidas, A., Zhang, J., & Cheng X. 2012, ApJ, 756, 143

Patsourakos, S., & Vourlidas, A. 2009, ApJ, 700, L182

Patsourakos, S., & Vourlidas, A. 2012, Sol. Phys., 281, 187

Patsourakos, S., Voulidas, A., Wang, Y.-M., Stenborg, G., & Thernisien, A. 2009, Sol. Phys., 259, 49

Pesnell, W. D., Thompson, B. J., & Chamberlin, P. C. 2012, Sol. Phys., 275, 3

Podladchikova, O., & Berghmans, D. 2005, Sol. Phys., 228, 265

Schmidt, J. M., & Ofman, L., 2010, ApJ, 713, 1008

Schrijver, C. J., Aulanier, G., Title, A. M., Pariat, E., & Delannée, C. 2011, ApJ, 738, 167

Shen, Y. D., & Liu Y., 2012, ApJ, 754, 7

Tian, H., McIntosh, S. W., De Pontieu, B., et al. 2011, ApJ, 738, 18

Thompson, B. J., Gurman, J. B., Neupert, W. M., et al. 1999, ApJ, 517, L151

Thompson, B. J., Plunkett, S. P., Gurman, J. B., et al. 1998, Geophys. Res. Lett., 25, 2465

Thompson, B. J., & Myers, D. C. 2009, ApJS, 183, 225

Veronig, A. M., Gömöry, P., Kienreich, L. W., et al. 2011, ApJ, 743, L10

Veronig, A. M., Temmer, M., & Vršnak, B. 2008, ApJ, 681, L113

Veronig, A. M., Temmer, M., Vršnak, B., & Thalmann, J. K. 2006, ApJ, 647, 1466

Uchida, Y. 1968, Sol. Phys., 4, 30

Wang, H., Shen, C., & Lin, J. 2009a, ApJ, 700, 1716

Wang, T. J., Ofman, L., & Davila, J. M. 2009b, ApJ, 696, 1448

Wang, Y.-M. 2000, ApJ, 543, L89

Warmuth, A. 2010, Advances in Space Research, 45, 527

Warmuth, A., & Mann, G. 2011, A&A, 532, A151

Warmuth, A., Vršnak, B., Aurass, H., & Hanslmeier, A. 2001, ApJ, 560, L105

Warmuth, A., Vršnak, B., Magdalenić, J., Hanslmeier, A., & Otruba, W. 2004, A&A, 418, 1117

West, M. J., Zhukov, A. N., Dolla, L., & Rodriguez, L. 2011, ApJ, 730, 122

Wills-Davey, M. J., & Attrill, G. D. R. 2009, Space Sci. Rev., 149, 325

Wills-Davey, M. J., DeForest, C. E., & Stenflo, J. O. 2007, ApJ, 664, 556

Wills-Davey, M. J., & Thompson, B. J. 1999, Sol. Phys., 190, 467

Wu, S. T., Zheng, H., Wang, S., et al. 2001, J. Geophys. Res., 106, 25089

Wuelser, J. P., Lemen, J. R., Tarbell, T. D., et al. 2004, Proc. SPIE, 5171, 111

Zheng, R. S., Jiang, Y. C., Hong, J. C., et al. 2011, ApJ, 739, L39

Zhukov, A. N. 2011, Journal of Atmospheric and Solar-Terrestrial Physics, 73, 1096

Zhukov, A. N., & Auchère, F. 2004, A&A, 427, 705

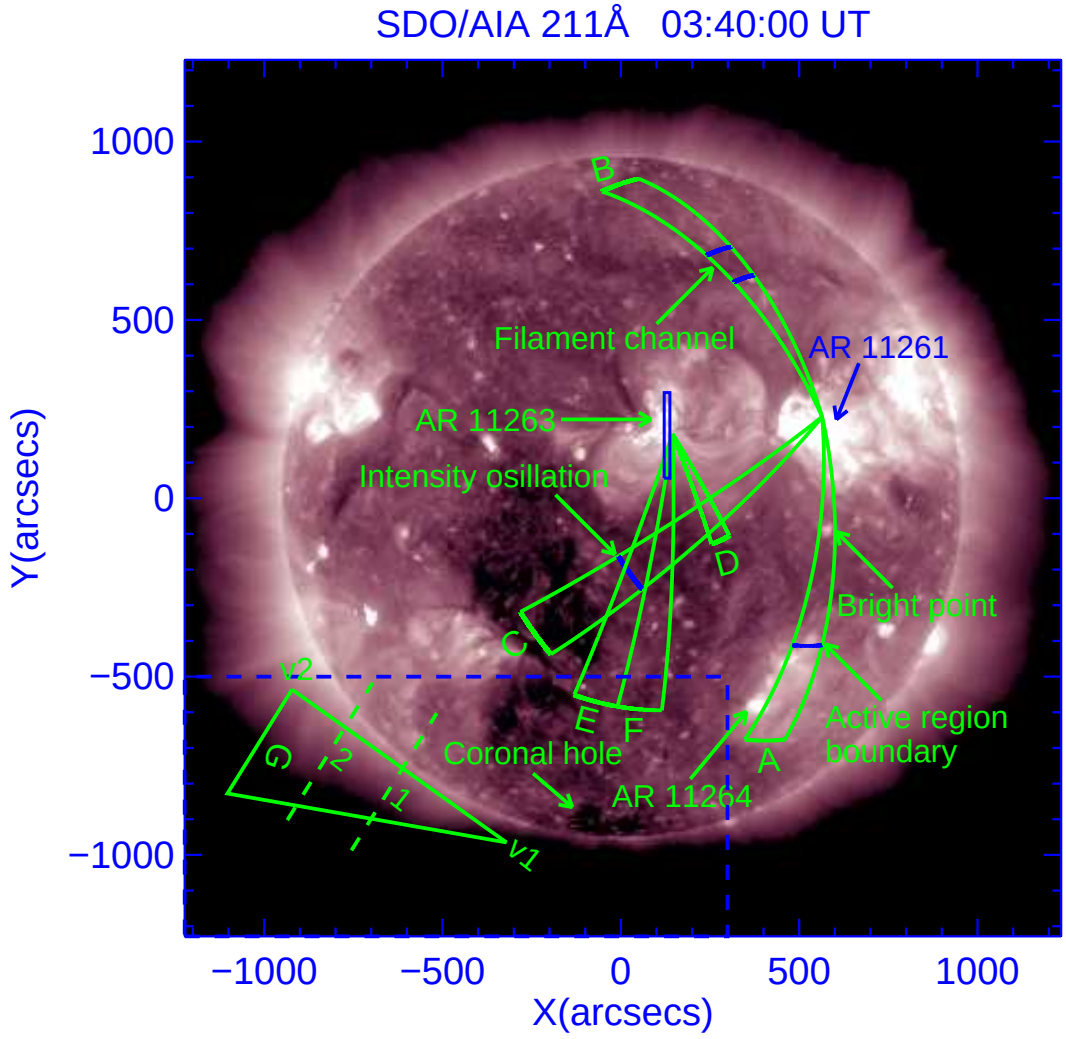

Fig. 1.— Six 10° wide sectors ("A"–"F") and one triangular sector ("G") displayed on an *SDO*/AIA 211 Å full-disk image which are used to obtain space-time plots in Figures 3–6.

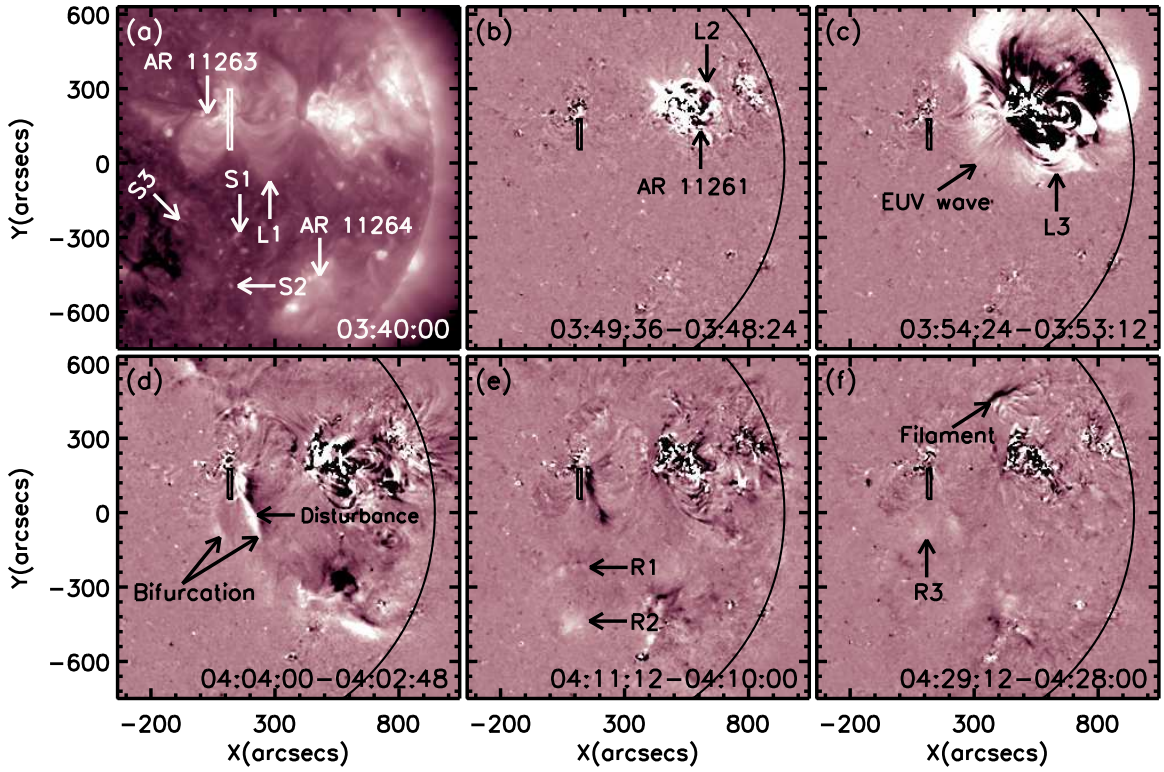

Fig. 2.— Sequences of *SDO*/AIA 211 Å direct (a) and running difference images ((b)–(f)) showing the propagation of the EUV wave. The white box in (a) indicates the position of the *Hinode*/EIS spectrometer slit. The field of view (FOV) of Figure 7 is marked by black boxes in (b)–(f). "L1" denotes AR loops connecting AR 11261 and AR 11263. "L2" and "L3" are expanding loops during the EUV wave transit. "S1", "S2" and "S3" represent three coronal structures producing reflected waves, and "R1", "R2" and "R3" correspond to the reflected waves. The black curve in (b)–(f) marks the limb of the solar disk. The FOV is 1380″×1380″.

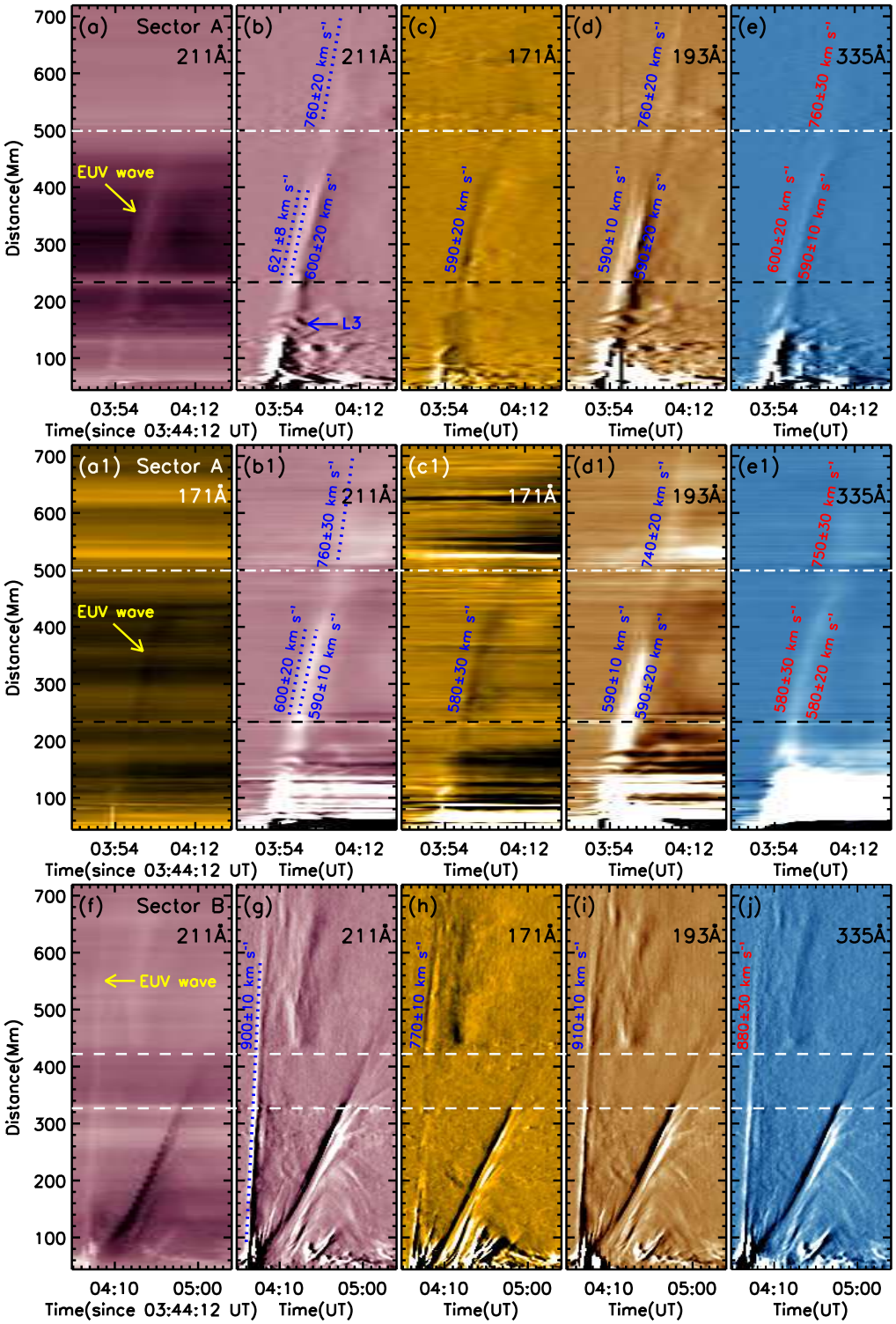

Fig. 3.— Original ((a) and (f)), base ((b1)–(e1)) and running ((b)–(e) and (g)–(j)) difference space-time plots along Sectors "A" and "B" at 211, 171, 193 and 335 Å. Original space-time plot along Sector "A" at 171 Å is shown in (a1). "L3" denotes expanding loops during the EUV wave transit.

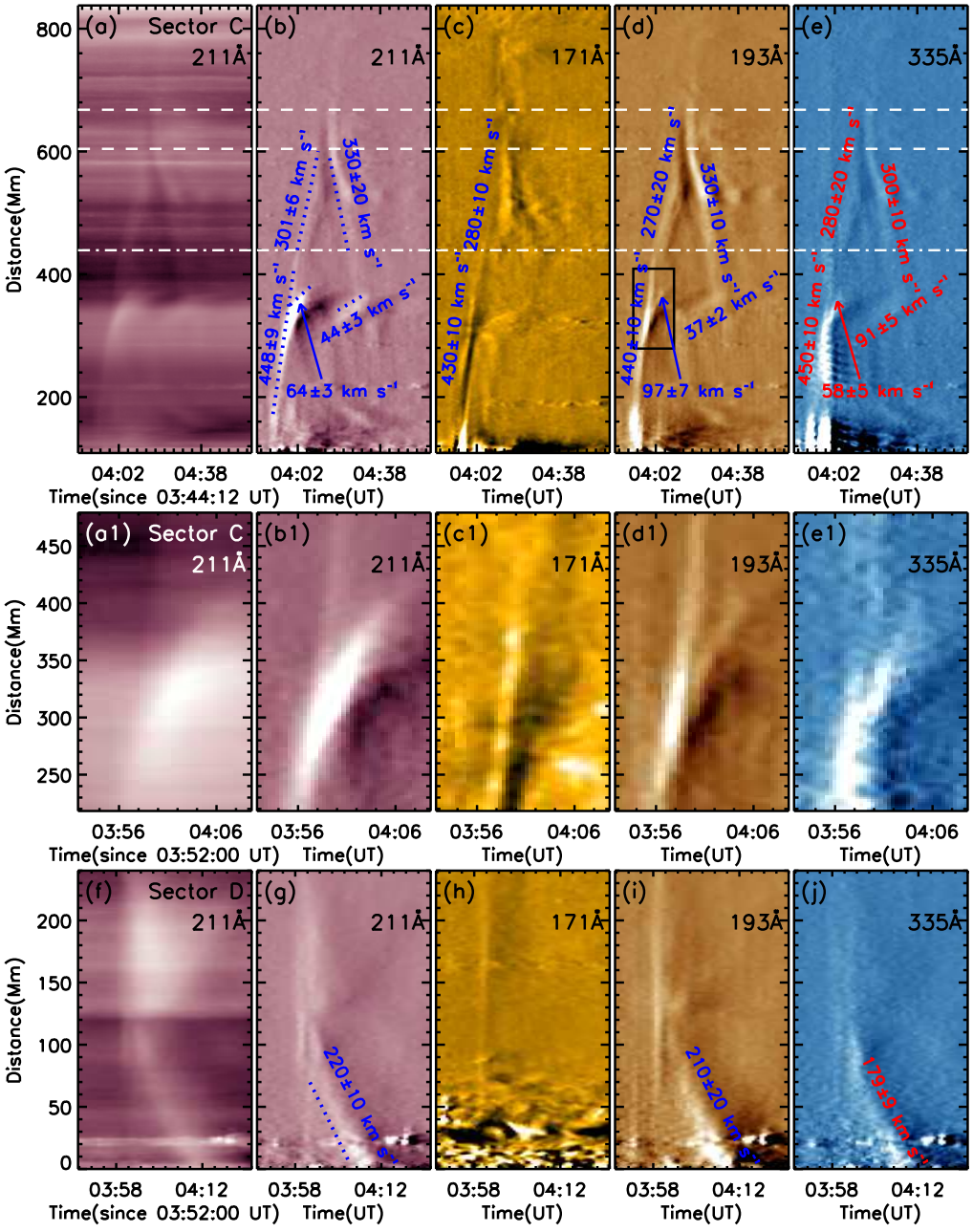

Fig. 4.— Original (Column 1) and running difference (Columns 2–5) space-time plots along Sectors "C" and "D" at 211, 171, 193 and 335 Å. The black box in panel (d) indicates the FOV of panels (a1)–(e1).

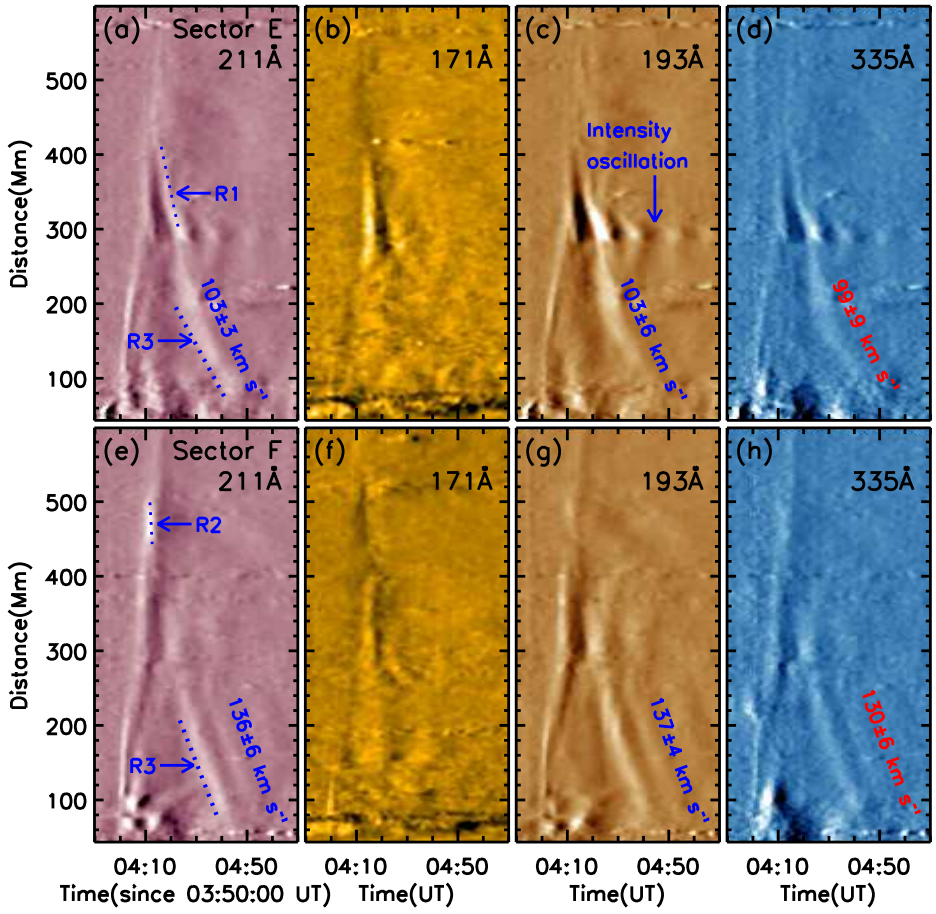

Fig. 5.— Running difference space-time plots along Sectors “E” and “F” at 211, 171, 193 and 335 Å.

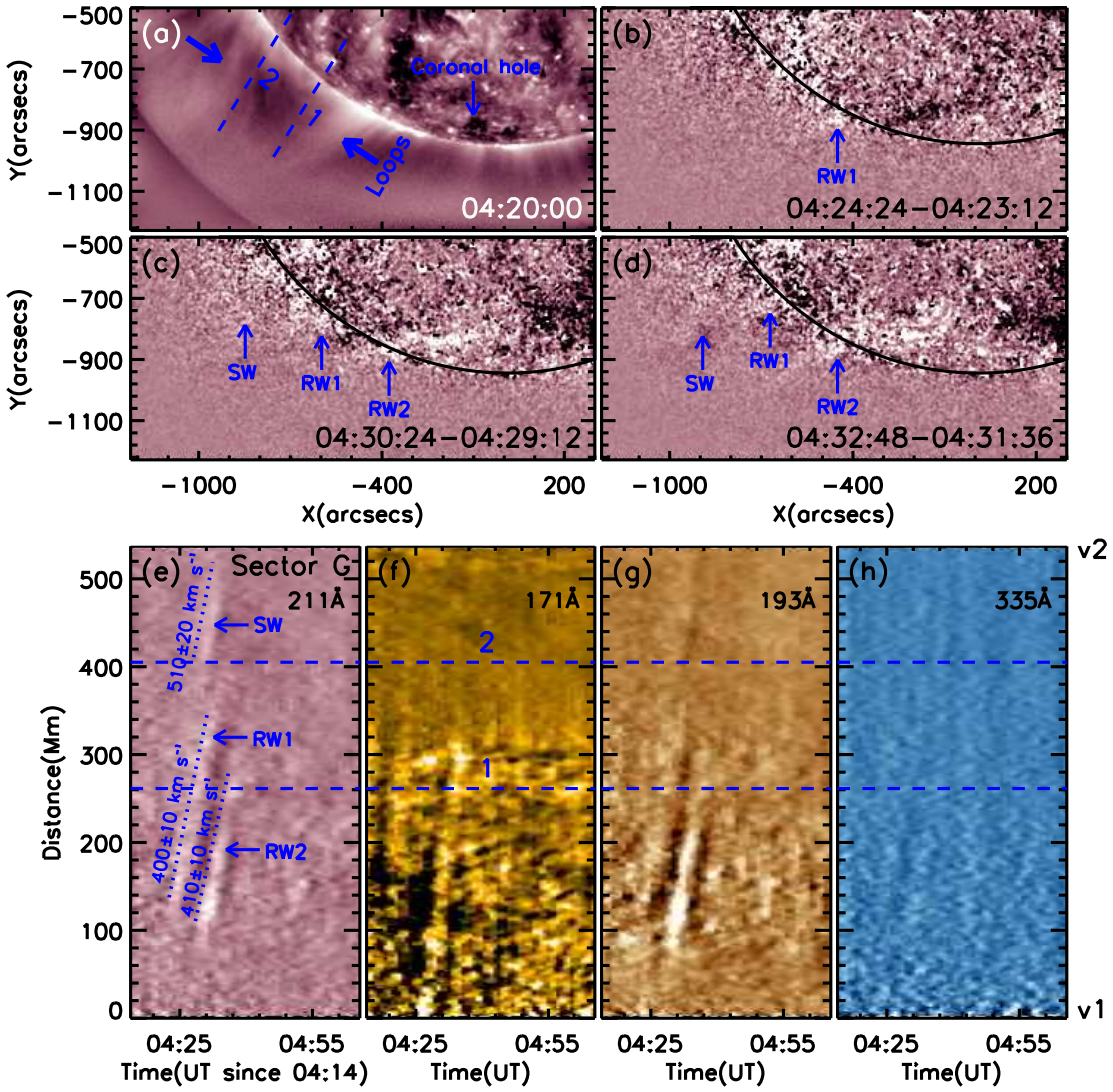

Fig. 6.— Sequences of *SDO*/AIA 211 Å direct (a) and running difference ((b)–(d)) images showing the two reflected waves of the southern polar CH and the newly produced secondary wave. The FOV is indicated by the rectangle in Figure 1. Running difference space-time plots ((e)–(h)) are along the Sector "G" at 211, 171, 193 and 335 Å.

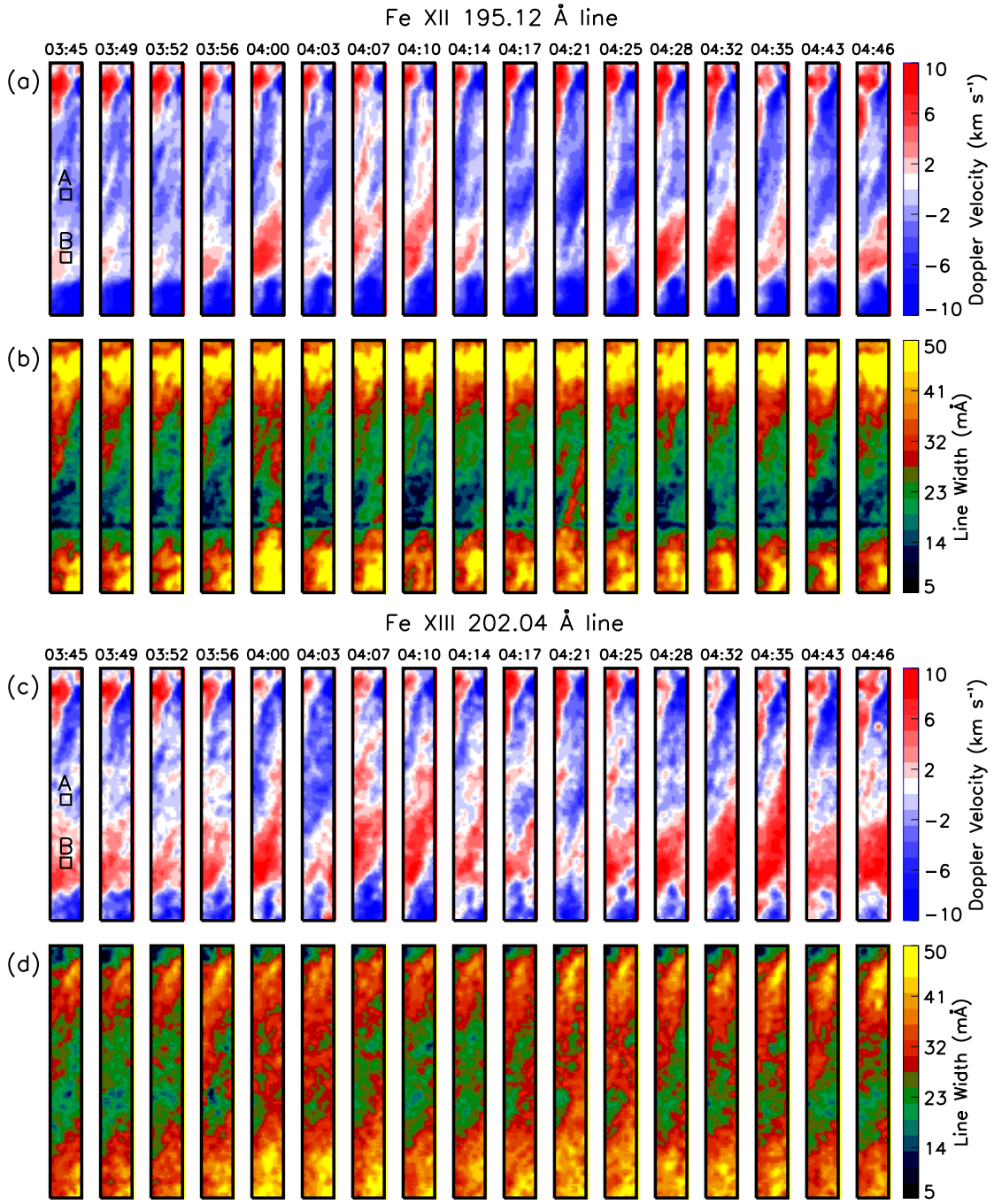

Fig. 7.— Time sequences of Doppler velocity ((a) and (c)) and line width ((b) and (d)) images for the Fe XII 195.12 Å and Fe XIII 202.04 Å lines. "A" and "B" are two regions where averaged Doppler velocity and line width are calculated in Figure 8. The FOV is $16'' \times 120''$.

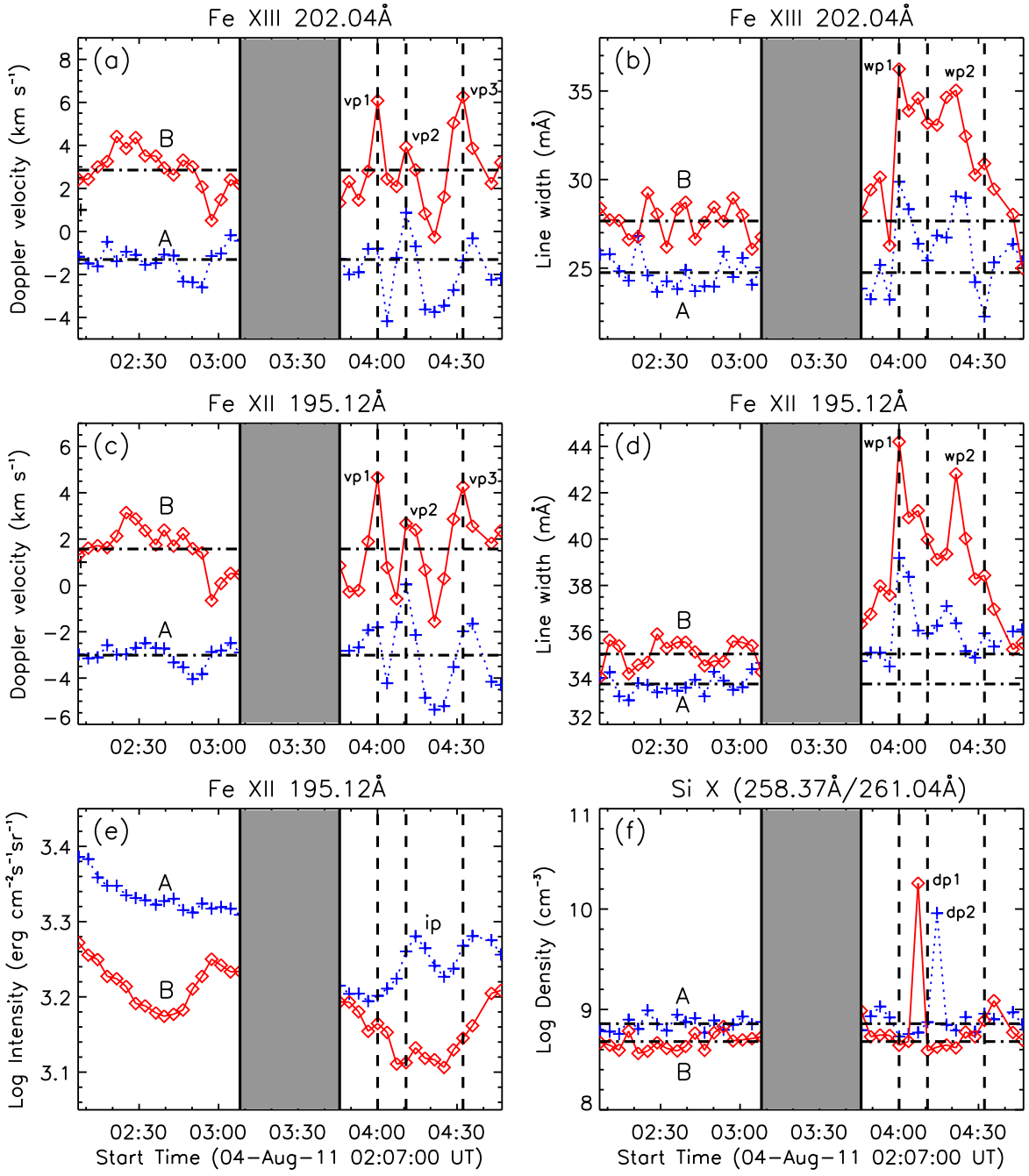

Fig. 8.— Averaged Doppler velocity ((a) and (c)), line width ((b) and (d)), line intensity (e) and plasma density (f) (calculated within "A" and "B" in Figure 7) as a function of time. "vp1", "vp2" and "vp3" represent the three peaks of Doppler velocity. "wp1" and "wp2" denote the two peaks of line width. "dp1" and "dp2" represent the two peaks of density, and "ip" denotes the peak of line intensity. The gray areas indicate that there are no data in the related time range. The horizontal dark dash-dotted lines represent the mean values of the Doppler velocity, line width and plasma density during the period between 02:07 and 03:08 UT.